Modeling multiaxial damage regional variation in human annulus fibrosus

Abderrahman Tamoud, Fahmi Zaïri, Amar Mesbah, Fahed Zaïri

Version of Record: https://www.sciencedirect.com/science/article/pii/S174270612100605X
Manuscript_fe68a34861ed9a3f4e1f770a4c60029c

Modeling multiaxial damage regional variation in human annulus fibrosus

Abderrahman Tamoud[a,b], Fahmi Zaïri[a*], Amar Mesbah[b], Fahed Zaïri[c]

[a]Lille University, Civil Engineering and geo-Environmental Laboratory (ULR 4515 LGCgE), 59000 Lille, France
[b]University of Sciences and Technology Houari Boumediene, Laboratory of Advanced Mechanics, 16111 Algiers, Algeria
[c]Ramsay Générale de Santé, Hôpital privé Le Bois, 59000 Lille, France

*Corresponding author.
E-mail address: fahmi.zairi@polytech-lille.fr

Abstract

In the present article, a fully three-dimensional human annulus fibrosus model is developed by considering the regional variation of the complex structural organization of collagen network at different scales to predict the regional anisotropic multiaxial damage of the intervertebral disc. The model parameters are identified using experimental data considering as elementary structural unit, the single annulus lamellae stretched till failure along the micro-sized collagen fibers. The multi-layered lamellar/inter-lamellar annulus model is constructed by considering the effective interactions between adjacent layers and the chemical-induced volumetric strain. The regional dependent model predictions are analyzed under various loading modes and compared to experimental data when available. The stretching along the circumferential and radial directions till failure serves to check the predictive capacities of the annulus model. Model results under simple shear, biaxial stretching and plane-strain compression are further presented and discussed. Finally, a full disc model is constructed using the regional annulus model and simulations are presented to assess the most likely failed areas under disc axial compression.

Keywords: Annulus fibrosus; Regional dependence; Multiscale structure; Multiaxial damage and failure.

1. Introduction

The annulus fibrosus of the intervertebral disc is probably one of the most extraordinary composites that the nature produces. The annulus soft tissues exhibit an organized structural arrangement of collagen network at different scales of hierarchical organization [1-5]. The detailed information was only appreciated very recently [6-13]. The structural arrangement of collagen network varies throughout the disc which leads to a regional variation of its mechanics. In this regards, various damage and failure mechanisms operate in the different disc regions [14-16]. In order to prevent all kinds of sudden disc injuries, it is necessary to understand the failure risks considering the regional variation under various static loading conditions. Fruitful experimental studies have been undertaken over the years allowing the assessment of the annulus intrinsic constitutive response in relation to disc region and mechanical loading [17-20]. Modeling multiaxial damage regional variation in annulus can provide a better understanding of the failure onset and location in the disc, beyond experimental observations. Modeling mechanics of the healthy annulus was developed in several papers considering different approaches as physically realistic as possible, to name a few recently published [21-29]. The quantitative prediction of the annulus damage is less reported. Damage criteria were proposed to predict annulus failure under different loading conditions [30-33]. Nevertheless, the interest of this approach is questionable because it is intrinsically decoupled from the intrinsic properties and disconnected from the real microstructure and its evolution. The progressive loss of collagen network integrity implies a damage accumulation in annulus [34]. Proper description of damage and failure requires to consider the latter that can be introduced in continuum-based models. Mengoni et al. [35] developed a damage model for the non-fibrillar matrix restricted to the anterior annulus stretched in the radial direction. Later, Gao et al. [36] and Ghezelbash et al. [37] proposed a

damage model considering only the collagen fibers failure as local damage event. Tamoud et al. [34] developed a damage model considering the multiscale failure due to network hierarchical organization. The chemical-induced volumetric effects on the structure-damage relation were also introduced to consider the hydration state effects. Nonetheless, our previous work in [34] disregards the regional variation while it is the prerequisite condition to any disc prediction. The directional effects due to the structural arrangement along with the regional dependence make damage prediction a challenging task that still remains largely an open issue. To date, no constitutive model has been proposed to predict the multiaxial mechanics of the annulus fibrosus while the regional dependence of the relation between structure and damage is taken into consideration.

The main objective of this work is to formulate a fully three-dimensional constitutive representation of the annulus fibrosus to capture the regional dependence of the structure-damage relation. In order to reproduce the multiaxial loadings as close as to those undergone in-vivo by the annulus fibrosus, the material representation considers the complex collagen network arrangement of each disc region. To consider the progressive deformation-induced changes in the tissue, the model introduces the stretch-induced network re-orientation as well as the network damage leading to final failure. The model is identified at the scale of single annulus lamellae stretched along the fibers main direction. The regional dependent model predictions are then analyzed under various loading modes at the scale of multi-lamellae and compared to experimental data when available. The human annulus constitutive model is finally used to predict the heterogeneous mechanics of a full disc model.

The outline of the present paper is as follows. The constitutive model is fully described in Section 2. Section 3 presents the constitutive model identification and predictions. Full disc model predictions are presented and discussed in Section 4. Finally, remarks and conclusions are given in Section 5.

The following notation is used throughout the text. Tensors and vectors are respectively denoted by normal boldfaced letters and italicized boldfaced letters, while scalars and individual components of vectors and tensors are denoted by normal italicized letters. The superposed dot designates the time derivative.

2. Model formulation

We propose here a two-step strategy consisting in single lamellae identification followed by multi-lamellae multiaxial predictions as illustrated in Fig. 1. The required model parameters are identified on axial tests performed along the micro-sized collagen fibers of single annulus lamellae extracted from the different disc regions (AO: Anterior-Outer, AI: Anterior-Inner, PI: Posterior-Inner, PO: Posterior-Outer). Beyond taking into account the regional effect, this identification strategy is a valuable difference with our previous work [34] in which the model identification had been performed at the scale of multi-lamellae. In this paper, after its identification at the scale of single lamellae, the model is then verified by comparing its prediction with the experimental data of multi-lamellae performed under multiaxial loading. Uniaxial (UA), simple shear (SS), biaxial (BA) and plane-strain compression (PSC) tests are all being considered.

2.1. Multiscale structure

The model considers the hierarchical organization of the solid phase starting from the nanoscale [12-13] as well as its regional variation. As schematically represented in Fig. 2, the disc annulus is a multiple-network medium in which the organization in terms of orientation and distribution is regional dependent. The annulus consists in concentric lamellae (LM) reinforced by micro-sized type-I oriented collagen fibers (OCF). Two adjacent LM are connected by an inter-lamellar (ILM) matrix. A network of nano-sized elastic fibers (NEF)

connects both two OCF and two adjacent LM between them [1, 4]. The network of OCF and NEF will be described geometrically with respect to the global benchmark of the disc, respectively, with the angle θ with respect to the circumferential direction and with the angle ψ with respect to the radial direction in the parallel plane of the fibers. Quantities and orientations of the constituents can be found in the Supplementary Information. The latter is based on well-documented papers for the four main disc regions [11-12, 17-18, 38-39].

2.2. Damaged free energy functions

The randomly oriented proteoglycan macromolecules of the extracellular matrix (ECM), the OCF and the (inter-fibrillar and inter-lamellar) NEF are all being considered to model the solid phase. Each individual component is assumed as isotropic, homogeneous, incompressible and hyperelastic body. During the mechanical loading, the initiation and propagation of damage occur through a continuous evolution over the entire loading history. A damage variable d is introduced to provide a mathematical description of the local damage events occurring within the collagen network. Their progressive evolution is given by an expression following a two-parameter Weibull statistical distribution governed by the internal stress:

$$d = 1 - \exp\left(-\left(\frac{\|\mathbf{P}\|}{\beta} \right)^{\alpha} \right) \tag{1}$$

in which α and β are two damage parameters and $\|\mathbf{P}\| = \sqrt{\mathrm{tr}\left(\mathbf{P}\mathbf{P}^{T}\right)}$ is the Frobenius norm of the effective first Piola-Kirchhoff stress $\mathbf{P}$ of the individual solid component (ECM, OCF and NEF).

The damage variable d varies between 0 for the virgin state and can increase up to 1 in the case of fully damaged (cracking) state. It is taken as a monotonic increasing function of loading, i.e. the damage is considered as an irreversible phenomenon without possible

recovery. Note that the anisotropy of the damage mechanisms developed in the annulus is due to the collagen network organization. The model is based on the general damage mechanics framework for the hyperelasticity theory that introduced hyperelastic laws derived from free energy functions [40-41]. The mechanical free energy W_{mech} is expressed as a function of the ECM free energy W_{ECM} and the collagen networks free energies W_θ and W_ψ:

$$W_{mech} = \left(1-d_{ECM}\right)\phi_{ECM}W_{ECM} + \left(1-d_\theta\right)\phi_{OCF}W_\theta + \sum_\psi \left(1-d_\psi\right)\phi_\psi W_\psi \tag{2}$$

where d_{ECM}, d_θ and d_ψ are the damage variables that degrade the internal stiffness of respective components, $\phi_{ECM} = \phi_{ECM\_0}/J_{chem}$ is the ECM volume fraction, $\phi_{OCF} = \phi_{OCF\_0}/J_{chem}$ is the OCF volume fraction, $\phi_\psi = \phi_\eta \phi_{NEF}$ is the fibrils volume fraction calculated using the NEF volume fraction $\phi_{NEF} = \phi_{NEF\_0}/J_{chem}$ in a layer and the volume fraction of fibril bundles ϕ_η in a layer dependent on η with $\sum_\eta \phi_\eta = 1$. The terms ϕ_{ECM_0}, ϕ_{OCF_0} and ϕ_{NEF_0} are the volume fractions at the chemical equilibrium state. The term J_{chem} is the chemical-induced volumetric change.

The set of free energies must be prescribed for each component of the solid phase. The simple Neo-Hookean formulation is employed for the ECM free energy W_{ECM}:

$$W_{ECM} = \frac{1}{2}G_{ECM}\left(\bar{I}_1 - 3\right) \tag{3}$$

in which G_{ECM} is the ECM shear modulus and $\bar{I}_1 = \mathrm{tr}\left(\mathbf{C}_{mech}\right)$ is the first stretch invariant of the right Cauchy-Green deformation[1] $\mathbf{C}_{mech} = \mathbf{F}_{mech}^T.\mathbf{F}_{mech}$.

The collagen response exhibits 'toe' and 'linear' regions as described in Fig. 3. The 'toe' region is due to the collagen straightening during stretching that is followed by the "linear"

[1] The chemo-mechanical coupling is considered by the multiplicative decomposition of the total deformation gradient $\mathbf{F} = \mathbf{F}_{chem}.\mathbf{F}_{mech}$ into chemically-induced volumetric and mechanical parts $\mathbf{F}_{chem}$ and $\mathbf{F}_{mech}$.

region when the undulations disappear. The free energies W_θ and W_ψ are expressed by two distinct relations below and above $\lambda^*_{\theta,\psi}$ to describe the transition between 'toe' and 'linear' regions:

$$W_{\theta,\psi} = H\left(\overline{I}_{4\theta,\psi} - 1\right)\left[\frac{1}{2}\frac{C_1}{C_2}\left(\exp\left(C_2\left(\overline{I}_{4\theta,\psi} - 1\right)^2\right) - 1\right)\right] \quad \lambda_{\theta,\psi} < \lambda^*_{\theta,\psi} \tag{4}$$

$$W_{\theta,\psi} = H\left(\overline{I}_{4\theta,\psi} - 1\right)\left[\frac{C_3}{2}\left(\overline{I}_{4\theta,\psi} - \overline{I}^*_{4\theta,\psi}\right)^2 + \zeta_{\theta,\psi}\left(\overline{I}_{4\theta,\psi} - \nu_{\theta,\psi}\right)\right] \quad \lambda_{\theta,\psi} \geq \lambda^*_{\theta,\psi} \tag{5}$$

where C_1, C_2 and C_3 are material constants, $H(\bullet)$ is the Heaviside function, $\zeta_{\theta,\psi}$ and $\nu_{\theta,\psi}$ are functions that ensure continuity between 'toe' and 'linear' regions:

$$\zeta_{\theta,\psi} = C_1\left(\overline{I}^*_{4\theta,\psi} - 1\right)\exp\left(C_2\left(\overline{I}^*_{4\theta,\psi} - 1\right)^2\right) \tag{6}$$

$$\nu_{\theta,\psi} = \overline{I}^*_{4\theta,\psi} - \frac{C_1}{2C_2\zeta_{\theta,\psi}}\left(\exp\left(C_2\left(\overline{I}^*_{4\theta,\psi} - 1\right)^2\right) - 1\right) \tag{7}$$

The fourth stretch invariants $\overline{I}_{4\theta}$ and $\overline{I}_{4\psi}$ are given by:

$$\overline{I}_{4\theta} = \boldsymbol{a}.\mathbf{C}_{mech}.\boldsymbol{a} = \lambda_\theta^2 \text{ and } \overline{I}_{4\psi} = \boldsymbol{b}.\mathbf{C}_{mech}.\boldsymbol{b} = \lambda_\psi^2 \tag{8}$$

where $\boldsymbol{a}$ and $\boldsymbol{b}$ are the unit vectors expressed in the Cartesian coordinates by:

$$\boldsymbol{a} = \cos\theta\,\boldsymbol{x} + \left|\sin\theta\right|\boldsymbol{y} \text{ and } \boldsymbol{b} = \left|\cos\theta\cos\psi\right|\boldsymbol{x} + \left|\sin\theta\cos\psi\right|\boldsymbol{y} + \sin\psi\,\boldsymbol{z} \tag{9}$$

The term $\overline{I}^*_{4\theta,\psi}$ is the fourth stretch invariant for $\lambda_{\theta,\psi} = \lambda^*_{\theta,\psi}$. The two angles follow the following geometrical relations to consider stretch-induced re-orientation of the OCF and NEF networks:

$$\tan(\theta) = \tan(\theta_0)\frac{\lambda_y}{\lambda_x} \text{ and } \tan(\psi) = \begin{cases} \dfrac{\lambda_z}{\lambda_f}\tan(\psi_0) & \psi_0 \leq 90° \\ 180° + \dfrac{\lambda_z}{\lambda_f}\tan(\psi_0) & \psi_0 > 90° \end{cases} \tag{10}$$

where θ_0 and ψ_0 are the angles in the initial configuration, λ_x, λ_y and λ_z are the principal stretches, respectively, in the circumferential (***x***), axial (***y***) and radial (***z***) directions, and λ_f is the stretch in the OCF direction. The re-orientation allows to update the fourth invariant by considering the current fibers orientation in the deformed configuration [20, 24, 42].

The hydration state of the annulus soft tissues due to internal fluid content variation by osmosis has a considerable effect on the disc mechanics [43-46] and especially on the failure response [47]. The chemical free energy W_{chem} takes the following form [28]:

$$W_{chem} = \phi_{fluid} \frac{1}{2} \frac{K_1}{K_2} \left(\exp\left(K_2 \varepsilon_{chem\_d}^2 \right) - 1 \right) \tag{11}$$

where $\phi_{fluid} = 1 - \phi_{ECM} - \phi_{OCF} - \phi_{FCN}$ is the volume fraction of the fluid phase, K_1 and K_2 are material constants, K_1 and K_1/K_2 being the initial and maximal volumetric stiffness values, respectively, and ε_{chem_d} is the damaged chemical-induced volumetric strain. The latter quantity must be connected to the damage accumulation due to progressive local failure events. The following relation is used [34]:

$$\varepsilon_{chem\_d} = \varepsilon_{chem} \left(1 - d_{ECM} \right) \left(1 - d_\theta \right) \left(1 - \frac{1}{n} \sum_{\psi}^{n} d_\psi \right) \tag{12}$$

with $\varepsilon_{chem} = \det\left(\mathbf{F}_{chem} \right) - 1$.

In virtue of the chemo-mechanical coupling, the total free energy W can be additively split into a mechanical part W_{mech} and a chemical part W_{chem}: $W = W_{mech} + W_{chem}$. The multi-layered lamellar/inter-lamellar annulus model is constructed by considering the compatibility conditions to be respected between adjacent layers. Some details are provided in the Supplementary Information.

3. Simulation vs. experiments

In this section, after its identification using available experimental data, the predictability of the above-described model is discussed. The constitutive equations were coded in MATLAB software and reduced to different loading forms.

3.1. Single lamellae identification

The intrinsic constitutive response of the annulus under UA loading was experimentally determined by Skaggs et al. [38] and Holzapfel et al. [39] on single annulus lamellae stretched along the fibers main direction. Fig. 4 shows the computed results for the identification of the OCF properties for the different disc regions. The identification was performed numerically using the MATLAB software to minimize the following objective function:

$$F_{stress}^{obj} = \frac{1}{\rho}\sum_{h=1}^{\rho}\left(\frac{P_{SLM}^{h} - \tilde{P}_{SLM}^{h}}{\tilde{P}_{SLM}^{h}}\right)^{2} \tag{13}$$

in which the letters with an overbar denote the experimental data with ρ the number of considered data points. Table 1 provides the obtained values for the OCF properties. Note that the regional dependence of the single lamellae stiffness is explained by a difference in the initial undulated state and the OCF content [38-39]. This structural difference is reflected by distinct values. The other model parameters are extracted from [34] and are listed in Table 2.

The simulated curves of the single lamellae are in good agreement with the experiments of Holzapfel et al. [39]. The results are shown until the complete loss of OCF load-bearing capability in order to compare the ultimate points with the experimental data of Skaggs et al. [38]. Except PI, it can be observed that the simulated stress and strain thresholds fall within the experimental standard deviation intervals.

3.2. Multi-lamellae multiaxial predictions

Table 3 presents the range of mechanical paths used to check the predictive capacities of the multi-lamellae model. It includes UA stretching in the circumferential direction, UA stretching in the radial direction, SS loading, BA stretching and PSC loading[2]. Except the latter loading (in which the sample is confined in the radial direction), the samples are loaded in specific directions while the others are free. All the samples are considered to be immersed in a physiological solution at a concentration of 0.15 M NaCl. When experimental data are available, a quantitative comparison with the model results is presented. The dimensions of the annulus specimens are given in Table 3 for the different loading conditions and disc regions.

The multi-lamellae predictions are presented in Figs. 5 and 6 for UA stretching along the circumferential direction. The simulated stress-stretch curves are compared with the typical experimental curves presented by Ebara et al. [18] in Fig. 5a. Considering the important variability in the experimental annulus response and that these experimental data are typical results (without statistical analysis), the model-experiments comparison can be considered as acceptable. In accordance with experiments, the outer regions have much higher stiffness than the inner regions, due mainly to regional variation in OCF angle. The simulations are conducted until stress drop corresponding to the failure stage. The simulated ultimate properties are reported in Fig. 5b and compared to the failure points with their standard deviation intervals extracted from the works of Acaroglu et al. [17] and Ebara et al. [18]. The failure strain predictions fail within the standard deviation intervals. Although the predicted failure stress can be found outside the experimental intervals, the predictive trends provide a regional difference in agreement with the experimental data. This important result confirms that the model provides a quite proper description of the regional effects on the relationship

[2] These different loadings are representative of the disc mechanics. UA stretching along the circumferential direction and PSC are representative of the disc axial compression [48]. UA stretching along the radial direction may be related to the disc shearing whereas SS may be related to the disc axial twist. BA stretching may be caused for example by a disc bending (i.e. flexion, extension and lateral flexion) [49].

between the actual microstructure, the damage events and the macroscopic ultimate properties. Recall that the model connects macroscopic response and hydration (volumetric) effects. The capacity of the model to capture the regional variation of the transverse responses is shown in Fig. 6. The LM-ILM interaction highlights the crucial role that the OCF regional orientations play in the transverse response [25]. In particular, regarding the possibility of an apparent auxeticity manifested by the positive transversal strains of the lamellae plane [50].

Thanks to the incorporation of the actual nanostructure materialized by the network of fibrils, the model can predict the regional behavior of the annulus in the radial direction. Fig. 7a shows the multi-lamellae stress-stretch responses under UA stretching along the radial direction. Again, the simulations are conducted until the appearance of the stress drop. The experimental data of Fujita et al. [19] are reported in Fig. 8 to further verify the model predictive capacities. Both moduli and ultimate properties fall within the experimental standard deviation intervals of Fujita et al. [19]. By taking into account accurately the connections between layers, the model allows also to predict the shearing resistance. Fig. 7b shows such predictions for which it can be observed a strong regional dependence. In addition to amount, type and orientation of the collagen network, the regional variation of the NEF arrangement leads to different predicted stiffness and failure thresholds according to the disc region. The connection of collagen network between lamellae from nanoscale made it possible to represent precisely the damage processes in the LM and ILM connections in the different annulus regions. The model shows that the different regional thresholds of radial and shear failures are caused by the regional arrangement of the NEF. These results are in agreement with the qualitative data analyzed in Fujita et al. [19]. Indeed, it was reported from image analysis that inter-layer connections such as NEF contribute to the annulus radial resistance [2, 51].

The directional effects are quite well captured by the model, especially the much higher stretchability along the radial direction than along the circumferential direction. The BA stress-strain responses are presented in Fig. 9 for different strain ratios (= circumferential strain : axial strain, {1:1, 1:2 and 2:1}). In order to further evidence the directional effects, Fig. 10 presents the PSC stress-stretch responses for different strain ratios. The strain ratio has an important effect on the stiffness and the ultimate properties, with a stronger effect on the axial properties than the circumferential ones. The posterior zones show higher stiffness than the anterior zones. That can be justified by the fact that the OCF angles are close to 45°, and that the forces are well shared according to the two loading directions (circumferential and axial). Although the location was not indicated in the paper of O'Connell et al. [20], it is satisfactory to observe that the BA predictions of the inner parts are in acceptable agreement with their typical experimental curves. The model indicates that the damage first initiates in the posterior zone. This result is actually found for all examined loading modes. PO has indeed a weak circumferential stretchability compared to other regions, as shown in UA stretching along the circumferential direction (see Fig. 5) and in BA stretching (see Fig. 7). That explains why PO exhibits a low ductility in PSC as observed in Fig. 10. Indeed, once PO reaches the circumferential failure, the axial failure occurs. As a consequence, PO shows a very low failure axial stress.

4. Full disc model

In this section, predictions of a full disc model are presented using the regional dependent constitutive representation of multi-lamellae and local damage mechanisms are clarified in order to get a basic insight about the starting areas of failure modes.

4.1. Disc construction and boundary conditions

A lot of finite element disc models were developed in the literature [26-27, 30-33, 52]. Beyond fundamental differences in the constitutive representation of the disc tissues, the time of model design and the time of calculation remain the main common weak points of all previous disc models. In the final objective to create time and cost-efficient patient-specific models of human discs, the present disc modeling strategy is purely analytical and again coded in MATLAB. The volume element of multi-lamellae, constitutively designed in the Cartesian space (x, y, z), was transferred to the Cylindrical space (r, θ, z) in order to consider the full disc geometry as illustrated in Fig. 11a. From the theoretical point of view, the constitutive equations were re-written within a finite-strain kinematic framework in Cylindrical coordinates. The reader is referred to the work of Holzapfel et al. [53] for the general theory on tube-like solid mechanics. In the present paper, we restrict the loading to a uniaxial compression at the disc external boundary. The disc is thus seen as a cylindrical solid loaded in compression on the superior surface and with a pressure in the cylindrical internal wall (Fig. 11b). The latter simulates the nucleus swelling applied to the internal wall of the disc annulus; the applied vertical axial displacement was translated to an internal pressure by considering the nucleus bulk modulus. The regional variation in structure and properties of the disc annulus was taken into account using the constitutive representation of each human annulus region. In order to ensure smooth transitions of the microstructural features (ECM, NEF, OCF and fluid) and properties from a disc annulus region to another, with a radial and circumferential variation, linear interpolations were considered using the data provided in the Supplementary Information. An angular increment $\delta\theta$ of 1° was chosen for the spatial discretization in the circumferential direction. Note that the number of layers determines the radial discretization.

An anatomically accurate three-dimensional model of a lumbar disc at the L1-L2 level was constructed using quantitative anatomical data taken from the work of Holzapfel et al. [39].

The L1-L2 disc geometric contours were approximated using special mathematical functions considering especially non-symmetric thicknesses and heights (Fig. 11a). Note that they may be adapted to consider the shape and size-changing with the spinal level and age [54]. The annulus was subdivided into 15 different lamellae (separated by 14 ILM zones) according to the L1-L2 disc dimensions provided by Holzapfel et al. [39]. The annulus size is considered to be approximately 50% of the disc volume [55]. It is worth noticing that a notable difference exists between in-vivo and in-vitro responses regarding fluid exudation. In-vivo, the healthy disc completely recovers its height and intradiscal pressure after long diurnal loading. In-vitro, several studies reported losses in the disc height and intradiscal pressure [46]. The chemical-induced volumetric strain was then affected by a multiplying factor. Several numerical simulations were performed with different values of the multiplying factor ranged from 0 to 100%, and a value of 50% was retained in the present work. During the simulations, a vertical axial displacement was applied on the superior surface while the inferior surface was constrained (Fig. 11b). The simulations were performed at a displacement rate of 0.01 mm/s in order to maintain quasi-static loading conditions.

4.2. Damage fields

The damage process in the disc core simulated by the model is recorded in Fig. 12 by differentiating the damage of the different solid constituents (ECM, NEF and OCF). That permits a better understanding of the origin of the damage mechanisms affecting the disc and existing at different scales, nanoscale for ECM proteoglycan macromolecules and for NEF network and microscale for OCF. A global view at the contour plots shows that damage progressively increases in intensity and in extent as the applied compression increases, which is accompanied by a disc volumetric change and an annulus-nucleus non-symmetric interaction. The different damage mechanisms may co-exist at the same time and initiate at

different locations. Remind that, in the present model, damage initiation and propagation are dependent on structure-property regional variation but also on the variation in displacement fields due to local differences in disc height. The highest damage zones in OCF are mainly observed in the anterior outer/lateral anterior ring. Excessive damage accumulation in these zones suggests the possibility of tear creation that may lead to an anterior herniation as experimentally reported in [14, 56-57]. Besides, the ECM and NEF damage patterns are presented in the two layers in order to appreciate the specific role of the ILM matrix and compare it to the adjacent LM. For both ECM and NEF, two critical zones appear in the lamellae on either side of the annulus with very low intensities. With relatively higher intensities, critical damage spots in the ILM matrix (for both ECM and NEF) are firstly located in the anterior side of the annulus and are then progressively more likely located in the neighborhood of the anterior inner part of the annulus. Quite interestingly, a confined distribution of the ILM damage can be observed in the lateral anterior inner and posterior inner sides of the annulus. The distribution of the fibrils in LM and in ILM makes the damage anisotropic. To illustrative this model capacity, the damage of the fibrils is plotted in Fig. 13 for two localities taken in posterior and anterior sides of the inner annulus (close to the annulus-nucleus interface), respectively, in LM and in ILM. The contour plots are plotted in a dial (90° representing the radial direction) in such a way that the directional effects can be observed during continuous loading. Whereas the damage in LM is confined to small degrees around the radial direction, with an onset at relatively important applied displacements and a relatively low intensity, the damage in ILM is developed earlier, it is more diffused and it is more intense. The damage in ILM is often judged as one of the most dangerous disc failure modes with the highest risk of disc delamination and failure propagation in the radial direction of the disc as experimentally reported in [14, 56-57].

5. Discussion and concluding remarks

In the present paper, a novel human annulus model was proposed to constitutively relate the regional variation in structural arrangement of collagen network at different scales and the multiaxial mechanics till failure. The model provides a useful tool to predict a variation of the annulus stiffness and ultimate properties with both disc region and loading mode. The different loading modes were simulated and chosen to better understand the regional behavior until the failure of the solid components in interaction with the chemical-induced volumetric response. The capabilities of the model were analyzed and an acceptable agreement between predicted values and experimental data was highlighted. A full disc model was constructed using the regional dependent constitutive representation of multi-lamellae and damage fields in the compressed disc were analyzed to assess the areas where the risk of failure is the highest.

The present model can be considered as the stepstone for the long-term prediction of the disc dysfunctions. During different complex loading scenarios of the spine, the disc dysfunctions may occur either by: i) mechanical damage due to a high level of loads [17-18] or relatively moderate loads repeated several times which cause damage accumulation [30, 33, 58-59], ii) by an age-related biological degeneration [60-62] or by the cellular disorders, including the cell death, the production of inflammatory mediators and a shift towards catabolism [63-65]. Nonetheless, it is difficult to identify or precisely model the disc failure taking into account the two causes of dysfunction at the same time. Since our study is based on the in-vitro annulus results, it cannot be directly extrapolated to the in-vivo disc response. Indeed, the understanding of the disc mechanobiology must be taken into account by the model considering especially nutrition and cellular activity along with degenerative aspects [63-65]. The model could be then a real help to provide solutions for remodeling and self-healing response of the disc tissues [66-69]. Moreover, the near-field direct local interactions within

the collagen network and the ECM ought to be treated through either the incorporation of a supplementary energy term [70] or a mean-field approach [71].

Acknowledgements

This work was financially supported by the PROFAS B+ Scholarships Program and the International Mobility Grants Program of the University of Lille.

References

[1] Yu, J., Peter, C., Roberts, S., Urban, J.P., 2002. Elastic fibre organization in the intervertebral discs of the bovine tail. Journal of Anatomy 201, 465-475.
[2] Pezowicz, C.A., Robertson, P.A., Broom, N.D., 2006. The structural basis of interlamellar cohesion in the intervertebral disc wall. Journal of Anatomy 208, 317-330.
[3] Pezowicz, C.A., Schechtman, H., Robertson, P.A., Broom, N.D., 2006. Mechanisms of anular failure resulting from excessive intradiscal pressure: a microstructural-micromechanical investigation. Spine 31, 2891-2903.
[4] Melrose, J., Smith, S.M., Appleyard, R.C., Little, C.B., 2008. Aggrecan, versican and type VI collagen are components of annular translamellar crossbridges in the intervertebral disc. European Spine Journal 17, 314-324.
[5] Schollum, M.L., Robertson, P.A., Broom, N.D., 2008. ISSLS prize winner: microstructure and mechanical disruption of the lumbar disc annulus: part I: a microscopic investigation of the translamellar bridging network. Spine 33, 2702-2710.
[6] Han, W.M., Nerurkar, N.L., Smith, L.J., Jacobs, N.T., Mauck, R.L., Elliott, D.M., 2012. Multi-scale structural and tensile mechanical response of annulus fibrosus to osmotic loading. Annals of Biomedical Engineering 40, 1610-1621.
[7] Yu, J., Schollum, M.L., Wade, K.R., Broom, N.D., Urban, J.P., 2015. A detailed examination of the elastic network leads to a new understanding of annulus fibrosus organization. Spine 40, 1149-1157.
[8] Vergari, C., Mansfield, J., Meakin, J.R., Winlove, P.C., 2016. Lamellar and fibre bundle mechanics of the annulus fibrosus in bovine intervertebral disc. Acta Biomaterialia 37, 14-20.
[9] Han, S.K., Chen, C.W., Labus, K.M., Puttlitz, C.M., Chen, Y., Hsieh, A.H., 2016. Optical coherence tomographic elastography reveals mesoscale shear strain inhomogeneities in the annulus fibrosus. Spine 41, 770-777.
[10] Tavakoli, J., Elliott, D.M., Costi, J.J., 2016. Structure and mechanical function of the inter-lamellar matrix of the annulus fibrosus in the disc. Journal of Orthopaedic Research 34, 1307-1315.
[11] Tavakoli, J., Elliott, D.M., Costi, J.J., 2017. The ultra-structural organization of the elastic network in the intra-and inter-lamellar matrix of the intervertebral disc. Acta Biomaterialia 58, 269-277.
[12] Tavakoli, J., Diwan, A.D., Tipper, J.L., 2020. The ultrastructural organization of elastic fibers at the interface of the nucleus and annulus of the intervertebral disk. Acta Biomaterialia 114, 323-332.
[13] Tavakoli, J., Diwan, A.D., Tipper, J.L., 2020. Elastic fibers: the missing key to improve engineering concepts for reconstruction of the nucleus pulposus in the intervertebral disc. Acta Biomaterialia 113, 407-416.

[14] Osti, O.L., Vernon-Roberts, B., Moore, R., Fraser, R.D., 1992. Annular tears and disc degeneration in the lumbar spine: a post-mortem study of 135 discs. The Journal of Bone and Joint Surgery 74, 678-682.
[15] Boos, N., Weissbach, S., Rohrbach, H., Weiler, C., Spratt, K.F., Nerlich, A.G., 2002. Classification of age-related changes in lumbar intervertebral discs. Spine 27, 2631-2644.
[16] Vernon-Roberts, B., Moore, R.J., Fraser, R.D., 2007. The natural history of age-related disc degeneration: the pathology and sequelae of tears. Spine 32, 2797-2804.
[17] Acaroglu, E.R., Iatridis, J.C., Setton, L.A., Foster, R.J., Mow, V.C., Weidenbaum, M., 1995. Degeneration and aging affect the tensile behavior of human lumbar anulus fibrosus. Spine 20, 2690-2701.
[18] Ebara, S., Iatridis, J.C., Setton, L.A., Foster, R.J., Mow, V.C., Weidenbaum, M., 1996. Tensile properties of nondegenerate human lumbar anulus fibrosus. Spine 21, 452-461.
[19] Fujita, Y., Duncan, N.A., Lotz, J.C., 1997. Radial tensile properties of the lumbar annulus fibrosus are site and degeneration dependent. Journal of Orthopaedic Research 15, 814-819.
[20] O'Connell, G.D., Sen, S., Elliott, D.M., 2012. Human annulus fibrosus material properties from biaxial testing and constitutive modeling are altered with degeneration. Biomechanics and Modeling in Mechanobiology 11, 493-503.
[21] Derrouiche, A., Zaïri, F., Zaïri, F., 2019. A chemo-mechanical model for osmo-inelastic effects in the annulus fibrosus. Biomechanics and Modeling in Mechanobiology 18, 1773-1790.
[22] Kandil, K., Zaïri, F., Derrouiche, A., Messager, T., Zaïri, F., 2019. Interlamellar-induced time-dependent response of intervertebral disc annulus: a microstructure-based chemo-viscoelastic model. Acta Biomaterialia 200, 75-91.
[23] Zhou, M., Bezci, S.E., O'Connell, G.D., 2019. Multiscale composite model of fiber-reinforced tissues with direct representation of sub-tissue properties. Biomechanics and Modeling in Mechanobiology 19, 745-759.
[24] Ghezelbash, F., Eskandari, A.H., Shirazi-Adl, A., Kazempour, M., Tavakoli, J., Baghani, M., Costi, J.J., 2021. Modeling of human intervertebral disc annulus fibrosus with complex multi-fiber networks. Acta Biomaterialia 123, 208-221.
[25] Kandil, K., Zaïri, F., Messager, T., Zaïri, F., 2020. Interlamellar matrix governs human annulus fibrosus multiaxial behavior. Scientific Reports 10, 19292.
[26] Castro, A.P.G., Alves, J.L., 2020. Numerical implementation of an osmo-poro-visco-hyperelastic finite element solver: application to the intervertebral disc. Computer Methods in Biomechanics and Biomedical Engineering 5, 538-550.
[27] Komeili, A., Rasoulian, A., Moghaddam, F., El-Rich, M., 2021. The importance of intervertebral disc material model on the prediction of mechanical function of the cervical spine. BMC Musculoskeletal Disorders 22, 1-12.
[28] Tamoud, A., Zaïri, F., Mesbah, A., Zaïri, F., 2021. A microstructure-based model for time-dependent mechanics of multi-layered soft tissues and its application to intervertebral disc annulus. Meccanica 56, 585-606.
[29] Zhou, M., Werbner, B., O'Connell, G.D., 2021. Fiber engagement accounts for geometry-dependent annulus fibrosus mechanics: a multiscale, structure-based finite element study. Journal of the Mechanical Behavior of Biomedical Materials 115, 104292.
[30] Qasim, M., Natarajan, R.N., An, H.S., Andersson, G.B.J., 2012. Initiation and progression of mechanical damage in the intervertebral disc under cyclic loading using continuum damage mechanics methodology: a finite element study. Journal of Biomechanics 45, 1934-1940.

[31] Qasim, M., Natarajan, R.N., An, H.S., Andersson, G.B.J., 2014. Damage accumulation location under cyclic loading in the lumbar disc shifts from inner annulus lamellae to peripheral annulus with increasing disc degeneration. Journal of Biomechanics 47, 24-31.
[32] Shahraki, N.M., Fatemi, A., Agarwal, A., Goel, V.K., 2015. Failure criteria for prediction of clinically relevant damage of annulus fibrosus. Spine Research 1, 7.
[33] Subramani, A.V., Whitley, P.E., Garimella, H.T., Kraft, R.H., 2020. Fatigue damage prediction in the annulus of cervical spine intervertebral discs using finite element analysis. Computer Methods in Biomechanics and Biomedical Engineering 23, 773-784.
[34] Tamoud, A., Zaïri, F., Mesbah, A., Zaïri, F., 2021. A multiscale and multiaxial model for anisotropic damage and failure of human annulus fibrosus. International Journal of Mechanical Sciences 205, 106558.
[35] Mengoni, M., Jones, A.C., Wilcox, R.K., 2016. Modelling the failure precursor mechanism of lamellar fibrous tissues, example of the annulus fibrosus. Journal of the Mechanical Behavior of Biomedical Materials 63, 265-272.
[36] Gao, X., Zhu, Q., Gu, W., 2017. An anisotropic multiphysics damage model with application to annulus fibrosus. Journal of Biomechanics 61, 88-93.
[37] Ghezelbash, F., Shirazi-Adl, A., Baghani, M., Eskandari, A.H., 2020. On the modeling of human intervertebral disc annulus fibrosus: Elastic, permanent deformation and failure responses. Journal of Biomechanics 102, 109463.
[38] Skaggs, D.L., Weidenbaum, M., Iatridis, J.C., Ratcliffe, A., Mow, V.C., 1994. Regional variation in tensile properties and biochemical composition of the human lumbar anulus fibrosus. Spine, 19, 1310-1319.
[39] Holzapfel, G.A., Schulze-Bauer, C.A.J., Feigl, G., Regitnig, P., 2005. Single lamellar mechanics of the human lumbar anulus fibrosus. Biomechanics and Modeling in Mechanobiology 3, 125-140.
[40] Lemaitre, J., Chaboche, J.L., 1994. Mechanics of Solid Materials. Cambridge University Press, Cambridge.
[41] Miehe, C., 1995. Discontinuous and continuous damage evolution in Ogden-type large strain elastic materials. European Journal of Mechanics - A/Solids 14, 697-720.
[42] Karsaj, I., Sansour, C., Soric, J., 2009. The modelling of fibre reorientation in soft tissue. Biomechanics and Modeling in Mechanobiology 8, 359-370.
[43] Derrouiche, A., Zaouali, A., Zaïri, F., Ismail, J., Chaabane, M., Qu, Z., Zaïri, F., 2019. Osmo-inelastic response of the intervertebral disc. Proceedings of the Institution of Mechanical Engineers. Part H: Journal of Engineering in Medicine 233, 332-341.
[44] Derrouiche, A., Feki, F., Zaïri, F., Taktak, R., Moulart, M., Qu, Z., Ismail, J., Charfi, S., Haddar, N., Zaïri, F., 2020. How pre-strain affects the chemo-torsional response of the intervertebral disc. Clinical Biomechanics 76, 105020.
[45] Yang, B., O'Connell, G.D., 2019. Intervertebral disc swelling maintains strain homeostasis throughout the annulus fibrosus: a finite element analysis of healthy and degenerated discs. Acta Biomaterialia, 100, 61-74.
[46] Feki, F., Taktak, R., Kandil, K., Derrouiche, A., Moulart, M., Haddar, N., Zaïri, F., Zaïri, F., 2020. How osmoviscoelastic coupling affects recovery of cyclically compressed intervertebral disc. Spine 45, 160553.
[47] Werbner, B., Spack, K., O'Connell, G.D., 2019. Bovine annulus fibrosus hydration affects rate-dependent failure mechanics in tension. Journal of Biomechanics 89, 34-39.
[48] Shah, J.S., Hampson, W.G., Jayson, M.I., 1978. The distribution of surface strain in the cadaveric lumbar spine. Journal of Bone and Joint Surgery 60, 246-251.
[49] Costi, J.J., Stokes, I.A., Gardner-Morse, M., Laible, J.P., Scoffone, H.M., Iatridis, J.C., 2007. Direct measurement of intervertebral disc maximum shear strain in six degrees of

freedom: motions that place disc tissue at risk of injury. Journal of Biomechanics 40, 2457-2466.
[50] Baldit, A., 2013. Etude des interactions hydro-chimio-mécaniques dans les tissus biologiques: application à la nutrition du disque intervertébral. Phd Thesis, University of Montpellier.
[51] Tavakoli, J., Costi, J.J., 2018. New findings confirm the viscoelastic behaviour of the inter-lamellar matrix of the disc annulus fibrosus in radial and circumferential directions of loading. Acta Biomaterialia 71, 411-419.
[52] Kandil, K., Zaïri, F., Messager, T., Zaïri, F., 2021. A microstructure-based model for a full lamellar-interlamellar displacement and shear strain mapping inside human intervertebral disc core. Computers in Biology and Medicine 135, 104629.
[53] Holzapfel, G.A., Gasser, T.C., Ogden, R.W., 2000. A new constitutive framework for arterial wall mechanics and a comparative study of material models. Journal of Elasticity and the Physical Science of Solids 61, 1-48.
[54] Amonoo-Kuofi, H.S., 1991. Morphometric changes in the heights and anteroposterior diameters of the lumbar intervertebral discs with age. Journal of Anatomy 175, 159-168.
[55] Violas, P., Estivalezes, E., Briot, J., Sales de Gauzy, J., Swider P., 2007. Objective quantification of intervertebral disc volume properties using MRI in idiopathic scoliosis surgery. Magnetic Resonance Imaging 25, 386-391.
[56] Schollum, M.L., Wade, K.R., Shan, Z., Robertson, P.A., Thambyah, A., Broom, N.D., 2018. The influence of concordant complex posture and loading rate on motion segment failure: a mechanical and microstructural investigation. Spine 43, E1116-E1126.
[57] Sapiee, N.H., Thambyah, A., Robertson, P.A., Broom, N.D., 2019. Sagittal alignment with downward slope of the lower lumbar motion segment influences its modes of failure in direct compression: A mechanical and microstructural investigation. Spine 44, 1118-1128.
[58] Green, T.P., Adams, M.A., Dolan, P., 1993. Tensile properties of the annulus fibrosus. European Spine Journal 2, 209-214.
[59] Iatridis, J.C., MacLean, J.J., Ryan, D.A., 2005. Mechanical damage to the intervertebral disc annulus fibrosus subjected to tensile loading. Journal of Biomechanics 38, 557-565.
[60] Thompson, J.P., Pearce, R.H., Schechter, M.T., Adams, M.E., Tsang, I.K., Bishop, P.B., 1990. Preliminary evaluation of a scheme for grading the gross morphology of the human intervertebral disc. Spine 15, 411-415.
[61] Urban, J.P., Roberts, S., 2003. Degeneration of the intervertebral disc. Arthritis Research & Therapy 5,120-130.
[62] Cegoñino, J., Moramarco, V., Calvo-Echenique, A., Pappalettere, C., Pérez del Palomar, A., 2014. A constitutive model for the annulus of human intervertebral disc: implications for developing a degeneration model and its influence on lumbar spine functioning. Journal of Applied Mathematics 2014, 1-15.
[63] Bruehlmann, S.B., Hulme, P.A., Duncan, N.A., 2004. In situ intercellular mechanics of the bovine outer annulus fibrosus subjected to biaxial strains. Journal of Biomechanics 37, 223-231.
[64] Walter, B.A., Korecki, C.L., Purmessur, D., Roughley, P.J., Michalek, A.J., Iatridis, J.C., 2011. Complex loading affects intervertebral disc mechanics and biology. Osteoarthritis and Cartilage 19, 1011-1018.
[65] Bloom, E.T., Lee, A.H., Elliott, D.M., 2021. Tendon multiscale structure, mechanics, and damage are affected by osmolarity of bath solution. Annals of Biomedical Engineering 49, 1058-1068.
[66] Likhitpanichkul, M., Dreischarf, M., Illien-Junger, S., Walter, B.A., Nukaga, T., Long, R. G., Sakai, D., Hecht, A.C., Iatridis, J.C., 2014. Fibrin-genipin adhesive hydrogel for

annulus fibrosus repair: performance evaluation with large animal organ culture, in situ biomechanics, and in vivo degradation tests. European Cells & Materials, 28, 25-38.
[67] Borde, B., Grunert, P., Härtl, R., Bonassar, L.J., 2015. Injectable, high-density collagen gels for annulus fibrosus repair: an in vitro rat tail model. Journal of Biomedical Materials Research Part A 103, 2571-2581.
[68] Wan, S., Borland, S., Richardson, S.M., Merry, C.L., Saiani, A., Gough, J.E., 2016. Self-assembling peptide hydrogel for intervertebral disc tissue engineering. Acta Biomaterialia, 46, 29-40.
[69] Peng, Y., Huang, D., Li, J., Liu, S., Qing, X., Shao, Z., 2020. Genipin-crosslinked decellularized annulus fibrosus hydrogels induces tissue-specific differentiation of bone mesenchymal stem cells and intervertebral disc regeneration. Journal of Tissue Engineering and Regenerative Medicine 14, 497-509.
[70] Guerin, H.L., Elliott, D.M., 2007. Quantifying the contributions of structure to annulus fibrosus mechanical function using a nonlinear, anisotropic, hyperelastic model. Journal of Orthopaedic Research 25, 508-516.
[71] Saadedine, M., Zaïri, F., Ouali, N., Tamoud, A., Mesbah, A., 2021. A micromechanics-based model for visco-super-elastic hydrogel-based nanocomposites. International Journal of Plasticity 144, 103042.

Table captions

Table 1. OCF parameters.

Table 2. ECM, NEF and swelling parameters.

Table 3. Loading modes for the multi-lamellae.

Figure captions

Figure 1. Two-step strategy consisting in annulus model identification using single lamellae extracted from different disc regions followed by multi-lamellae annulus model predictions for multiaxial elementary loading modes representative of the spine movement.

Figure 2. Multiscale view of the intervertebral disc annulus. The organization, in terms of orientation and distribution, of this multiple-network medium is regional dependent.

Figure 3. Phenomenon of reorientation of collagen fibers.

Figure 4. Single lamellae identification for the different disc regions: (a) stress-stretch responses (lines: model simulations, symbols: experimental data of Holzapfel et al. [39]), (b) ultimate properties (bars: model simulations, symbols with standard deviation intervals: experimental data of Skaggs et al. [38]).

Figure 5. Multi-lamellae UA predictions along circumferential direction for the different disc regions: (a) stress-stretch responses (lines: model simulations, symbols: experimental data of Ebara et al. [18]), (b) ultimate properties (bars: model simulations, square symbols with standard deviation intervals: experimental data of Ebara et al. [18], circle symbols with standard deviation intervals: experimental data of Acaroglu et al. [17]).

Figure 6. Multi-lamellae transverse responses under UA circumferential stretching for the different disc regions (solid lines: fibers plane, dashed lines: lamellae plane): (a) model results, (b) experimental data of Baldit [50].

Figure 7. Multi-lamellae stress-stretch responses under (a) UA radial stretching and (b) SS loading for the different disc regions (lines: model simulations, circle symbols: experimental data of Fujita et al. [19]).

Figure 8. Multi-lamellae UA predictions along radial direction for the different disc regions: (a) moduli, (b) ultimate properties (bars: model simulations, circle symbols with standard deviation intervals: experimental data of Fujita et al. [19]).

Figure 9. Multi-lamellae stress-stretch responses under BA stretching with various strain ratios for the different disc regions (lines: model simulations, circle symbols: experimental data of O'Connell et al. [20]).

Figure 10. Multi-lamellae stress-stretch responses under PSC loading with various strain ratios for the different disc regions.

Figure 11. Full disc model: (a) Passage from annulus constitutive model to anatomically accurate disc model including volumetric strain, regional and directional effects (disc dimensions at the L1-L2 level), (b) boundary conditions of the uniaxially compressed disc.

Figure 12. Damage contour plots in the superior view of the uniaxially compressed disc for different applied displacement levels (0.5, 1.0 and 1.5 mm); ECM damage d_{ECM} in LM and in ILM, NEF damage d_{NEF} in LM and in ILM, OCF damage d_{θ} in LM.

Figure 13. Damage of the fibrils in different directions (90° is the radial direction) at two zones of the uniaxially compressed disc: (a) posterior (in LM) and (b) anterior (in ILM) sides of the inner annulus for different applied displacement levels (from zero in the dial center to 2 mm in the dial boundary).

Parameters		Regions			
		AO	PO	AI	PI
C_1	$[\mathrm{MPa}]$	40	26	26	3
C_2	$[-]$	880	58	30	11
C_3	$[\mathrm{MPa}]$	500	300	400	80
λ_θ^*	$[-]$	1.02	1.07	1.1	1.14
α_{OCF}	$[-]$	5	5	5	5
β_{OCF}	$[\mathrm{MPa}]$	215	125	120	70

Table 1. OCF parameters.

Constituents	Parameters	Values	
ECM	G_{ECM}	0.01	$[\mathrm{MPa}]$
	α_{ECM}	2	$[-]$
	β_{ECM}	5.5	$[\mathrm{MPa}]$
NEF	C_1	12	$[\mathrm{MPa}]$
	C_2	0.2	$[-]$
	C_3	1.5	$[\mathrm{MPa}]$
	λ_ψ^*	1.7	$[-]$
	α_{NEF}	6	$[-]$
	β_{NEF}	400	$[\mathrm{MPa}]$
Swelling	K_1	0.14	$[\mathrm{MPa}]$
	K_2	0.0075	$[-]$

Table 2. ECM, NEF and swelling parameters.

Loading modes			Sample size $\left[mm^3\right]$		Experimental data
			Anterior	Posterior	
Uniaxial (UA)	Circ.	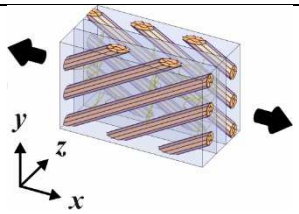	7×2×2	10×4×4	Ebara et al. [17] and Acaroglu et al. [18]
Uniaxial (UA)	Radial	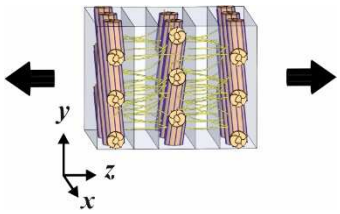	2×2×2	4×4×4	Fujita et al. [19]
Simple shear (SS)		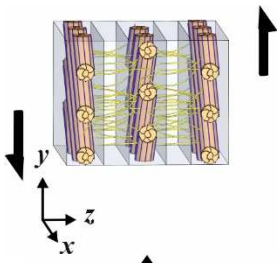	2×2×2	4×4×4	No available data
Biaxial (BA)	Axial-circ.	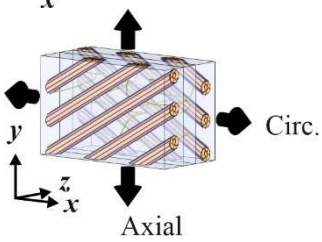	7×7×2	10×10×4	O'Connell et al. [20]
Plane-strain compression (PSC)	Axial-circ.	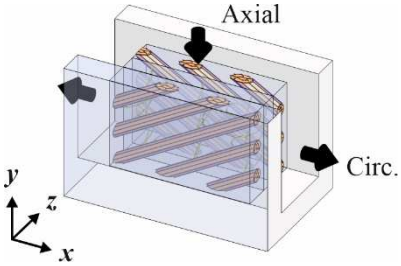	7×7×2	10×10×4	No available data

Table 3. Loading modes for the multi-lamellae.

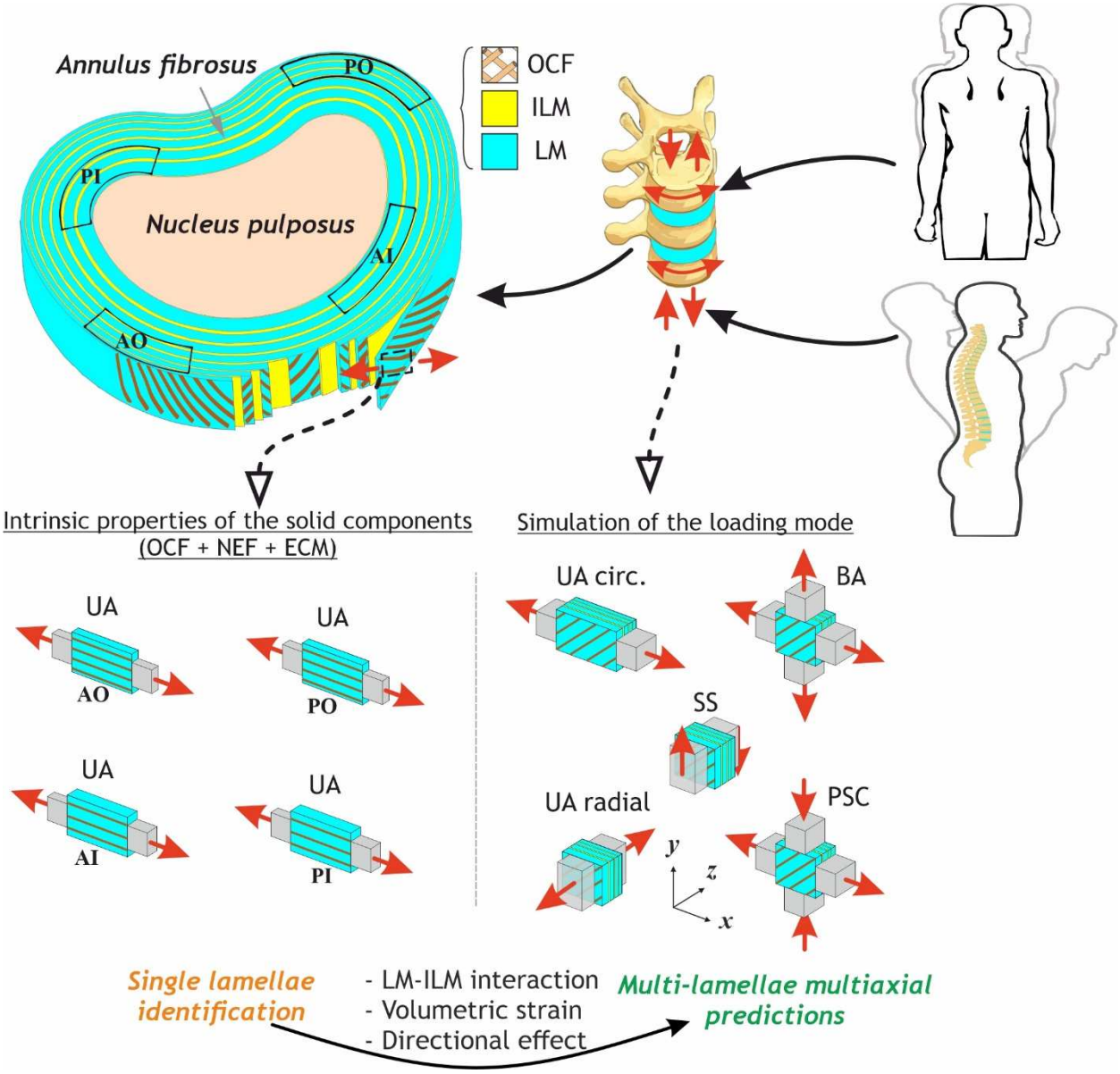

Figure 1. Two-step strategy consisting in annulus model identification using single lamellae extracted from different disc regions followed by multi-lamellae annulus model predictions for multiaxial elementary loading modes representative of the spine movement.

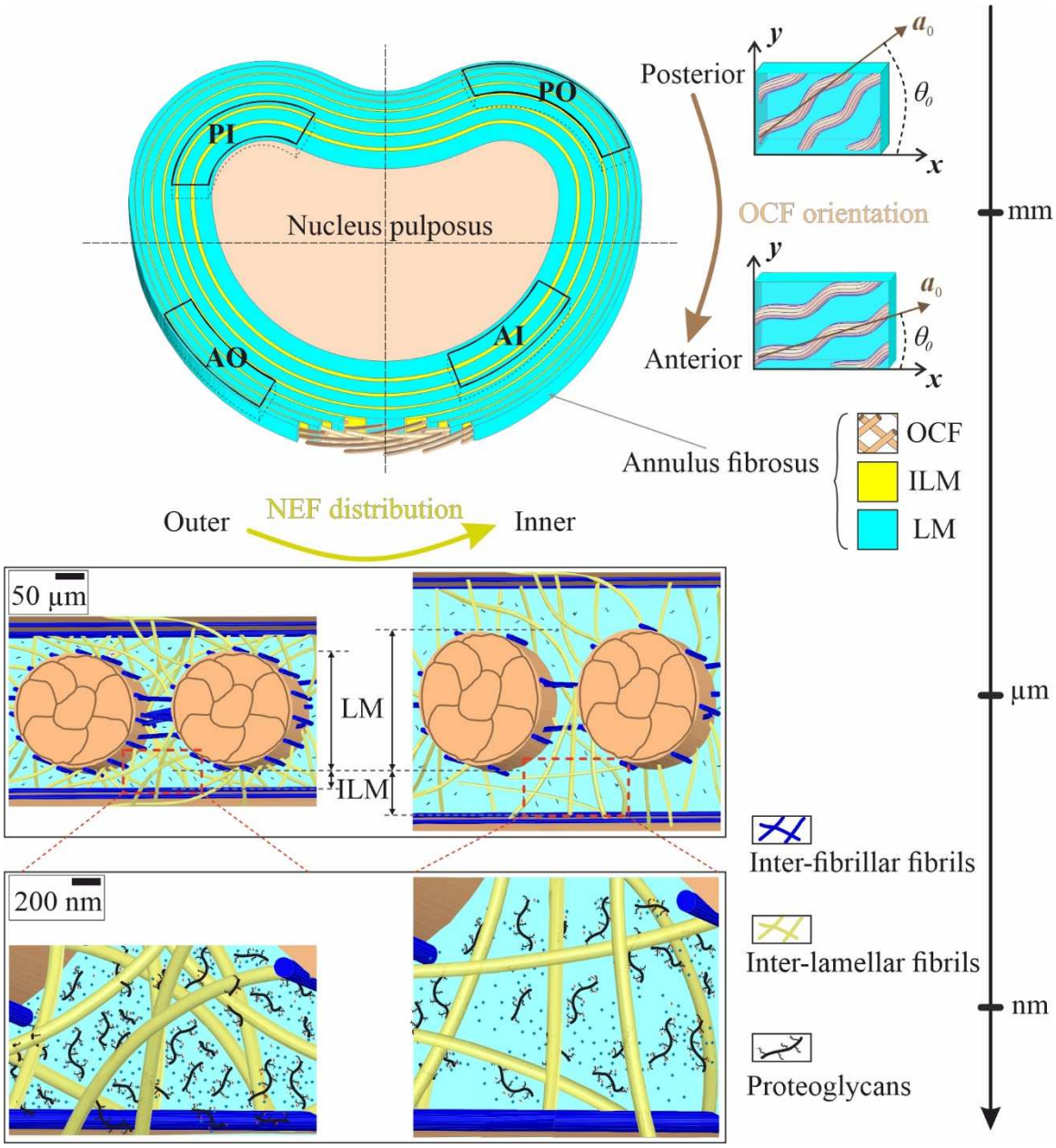

Figure 2. Multiscale view of the intervertebral disc annulus. The organization, in terms of orientation and distribution, of this multiple-network medium is regional dependent.

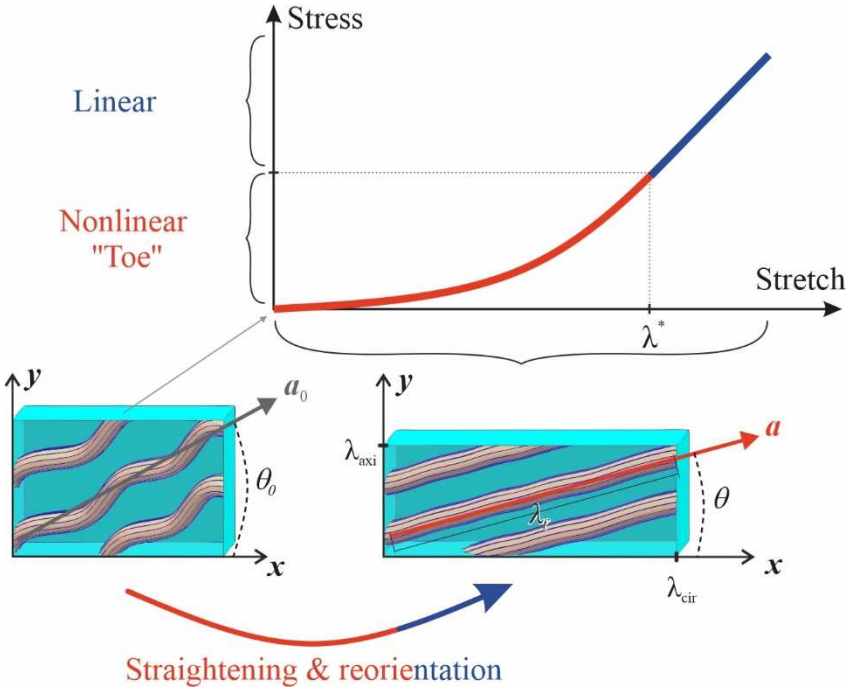

Figure 3. Phenomenon of reorientation of collagen fibers.

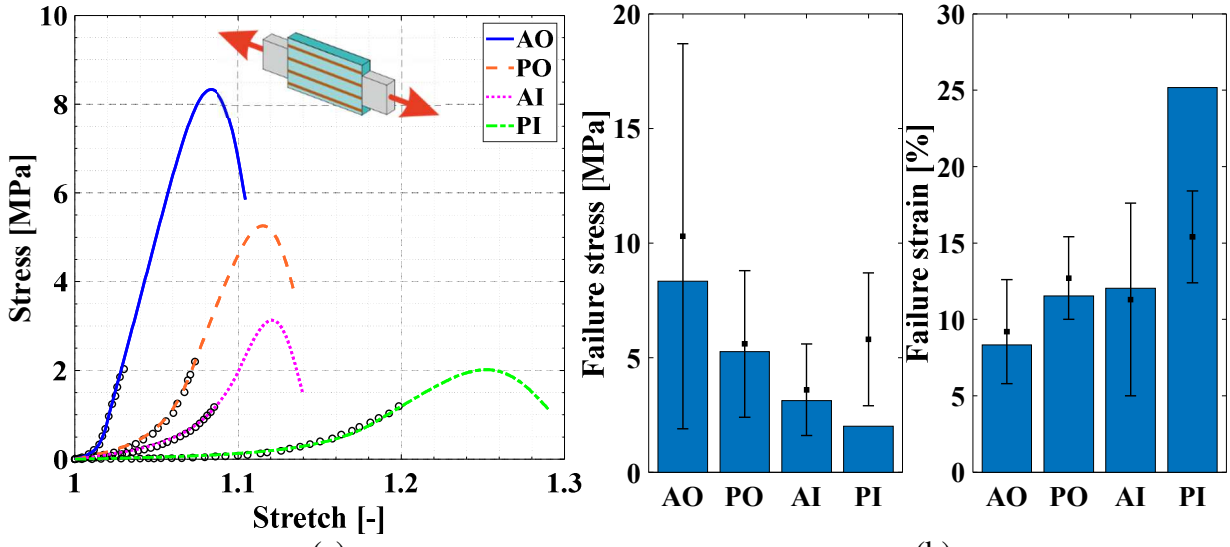

(a) (b)

Figure 4. Single lamellae identification for the different disc regions: (a) stress-stretch responses (lines: model simulations, symbols: experimental data of Holzapfel et al. [39]), (b) ultimate properties (bars: model simulations, symbols with standard deviation intervals: experimental data of Skaggs et al. [38]).

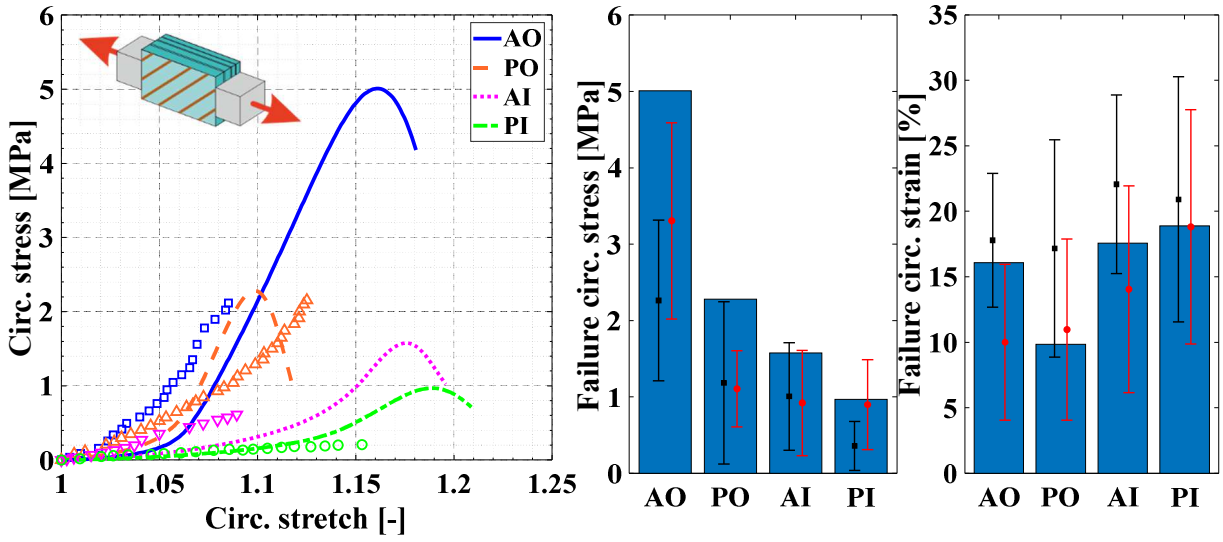

(a) (b)

Figure 5. Multi-lamellae UA predictions along circumferential direction for the different disc regions: (a) stress-stretch responses (lines: model simulations, symbols: experimental data of Ebara et al. [18]), (b) ultimate properties (bars: model simulations, square symbols with standard deviation intervals: experimental data of Ebara et al. [18], circle symbols with standard deviation intervals: experimental data of Acaroglu et al. [17]).

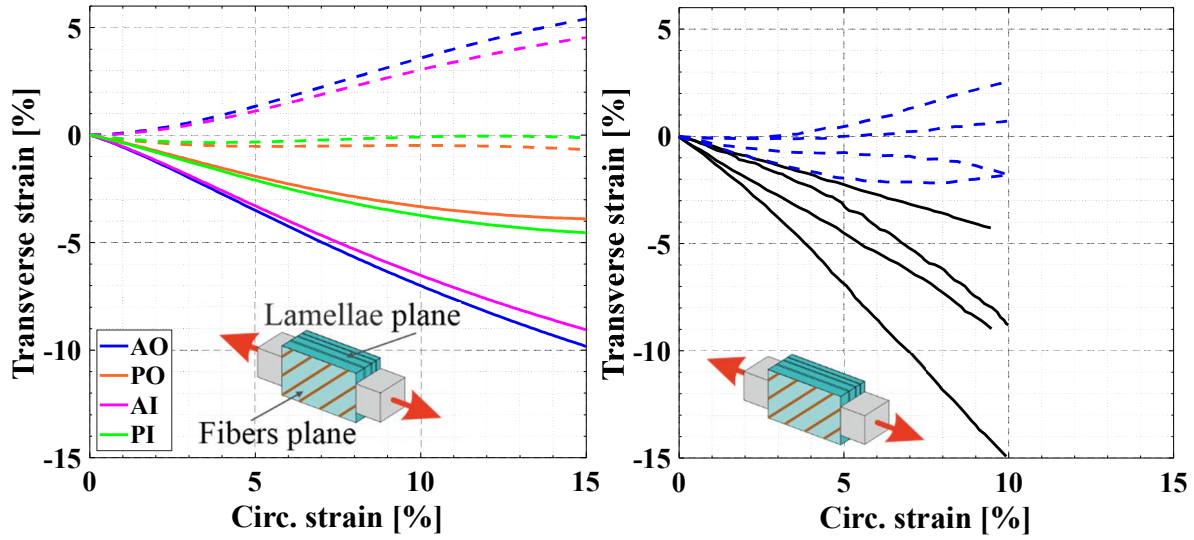

(a) (b)

Figure 6. Multi-lamellae transverse responses under UA circumferential stretching for the different disc regions (solid lines: fibers plane, dashed lines: lamellae plane): (a) model results, (b) experimental data of Baldit [50].

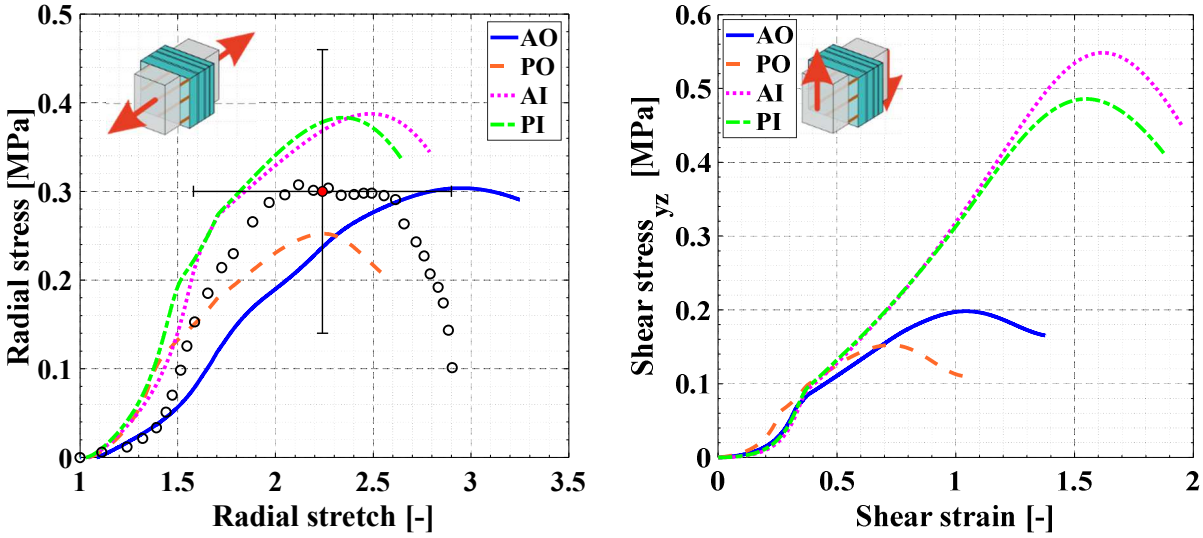

(a) (b)

Figure 7. Multi-lamellae stress-stretch responses under (a) UA radial stretching and (b) SS loading for the different disc regions (lines: model simulations, circle symbols: experimental data of Fujita et al. [19]).

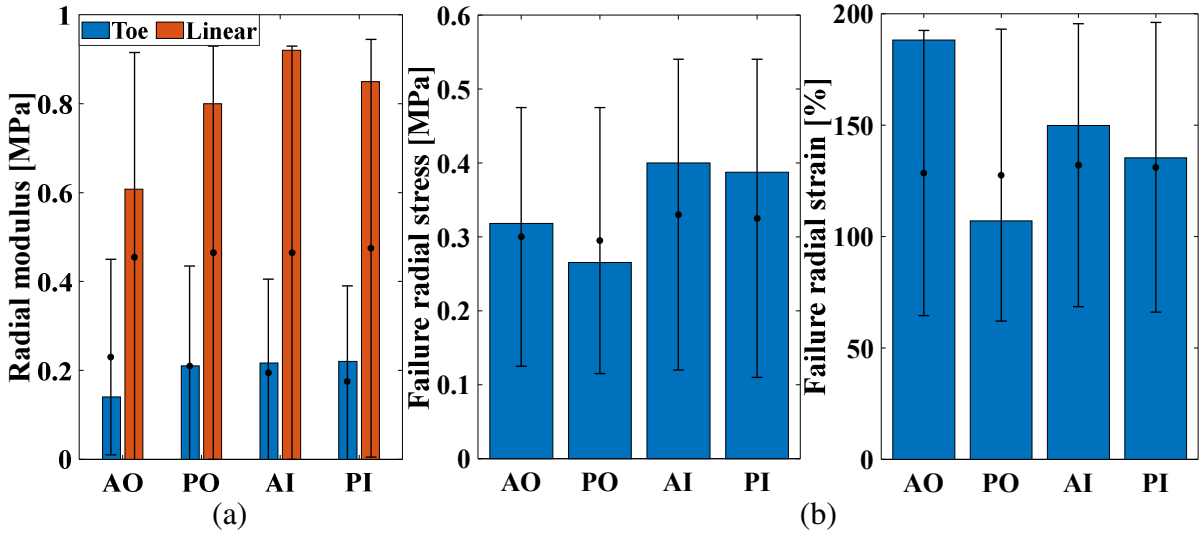

Figure 8. Multi-lamellae UA predictions along radial direction for the different disc regions: (a) moduli, (b) ultimate properties (bars: model simulations, circle symbols with standard deviation intervals: experimental data of Fujita et al. [19]).

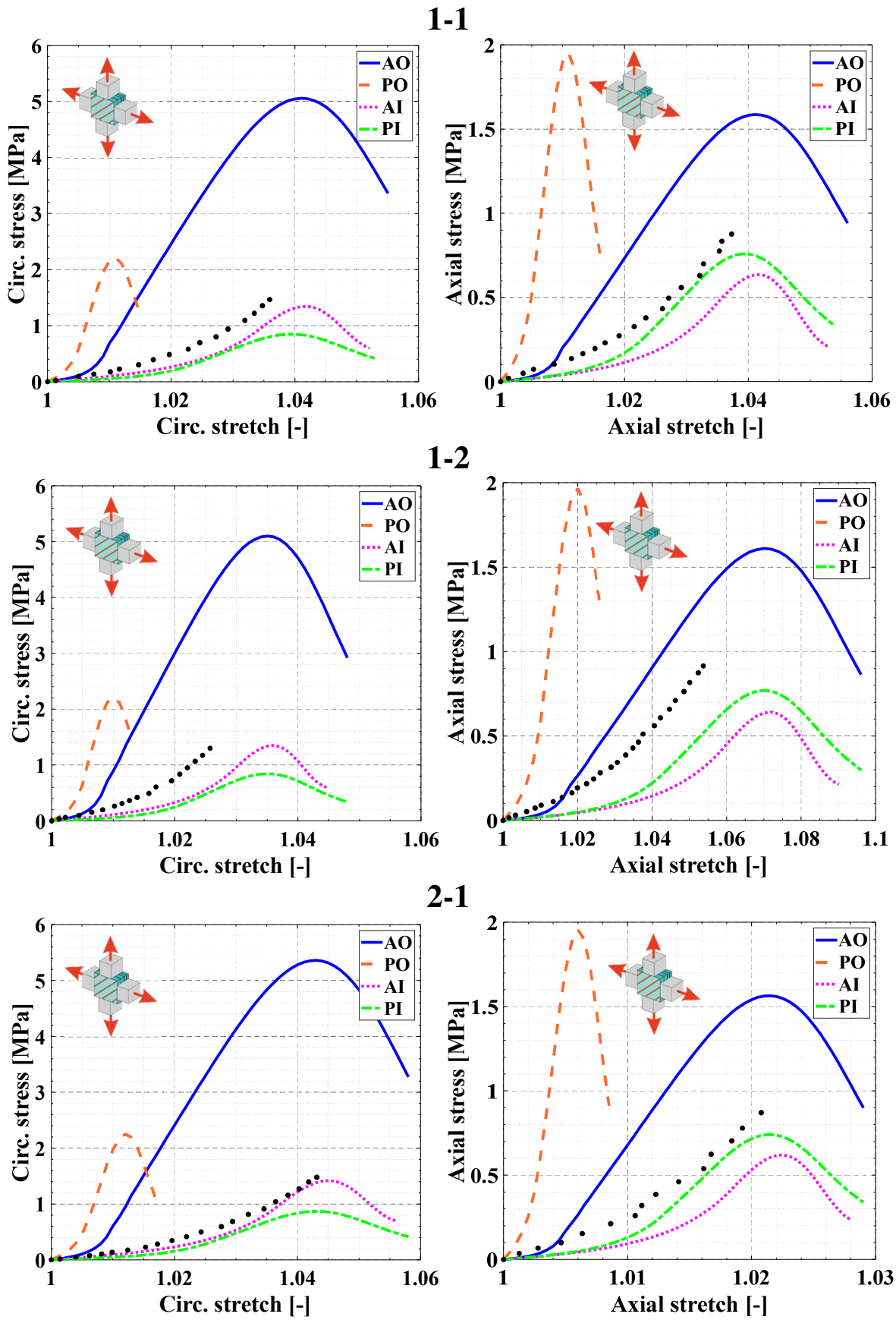

Figure 9. Multi-lamellae stress-stretch responses under BA stretching with various strain ratios for the different disc regions (lines: model simulations, circle symbols: experimental data of O'Connell et al. [20]).

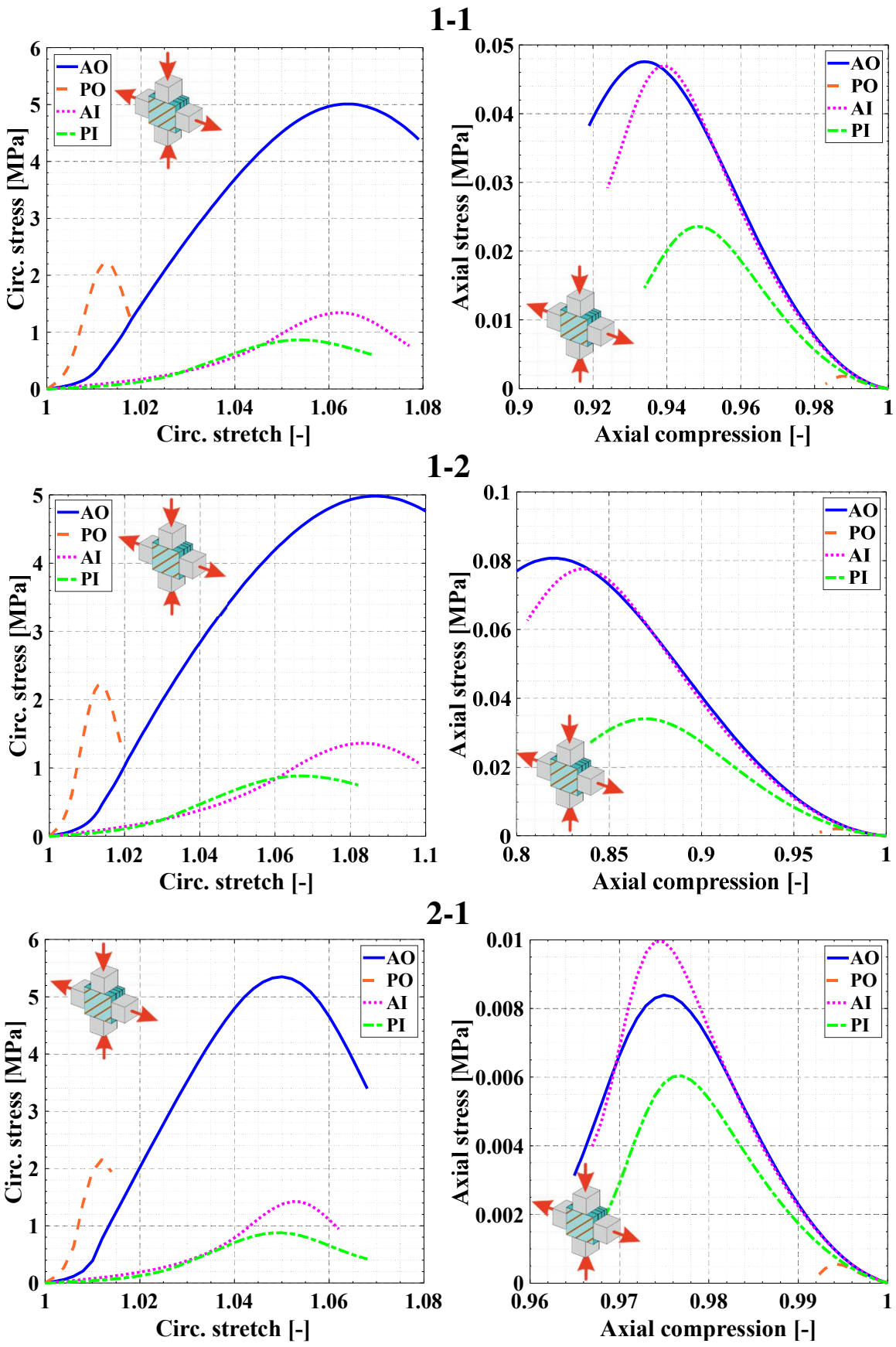

Figure 10. Multi-lamellae stress-stretch responses under PSC loading with various strain ratios for the different disc regions.

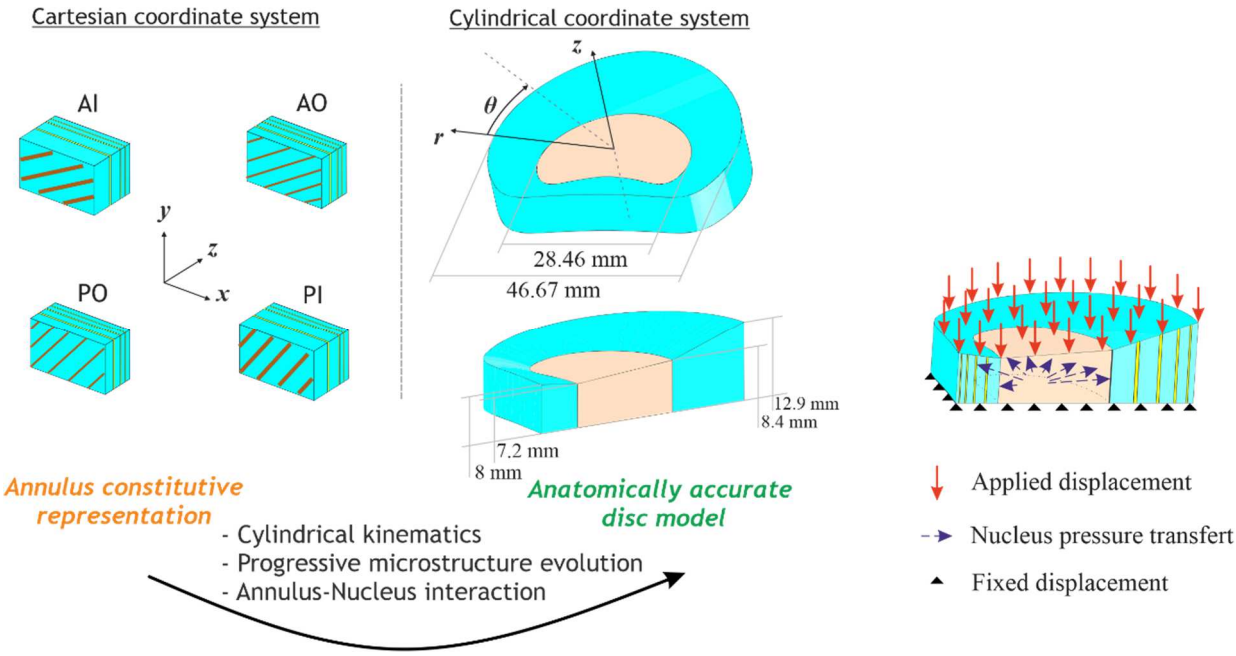

(a) (b)

Figure 11. Full disc model: (a) Passage from annulus constitutive model to anatomically accurate disc model including volumetric strain, regional and directional effects (disc dimensions at the L1-L2 level), (b) boundary conditions of the uniaxially compressed disc.

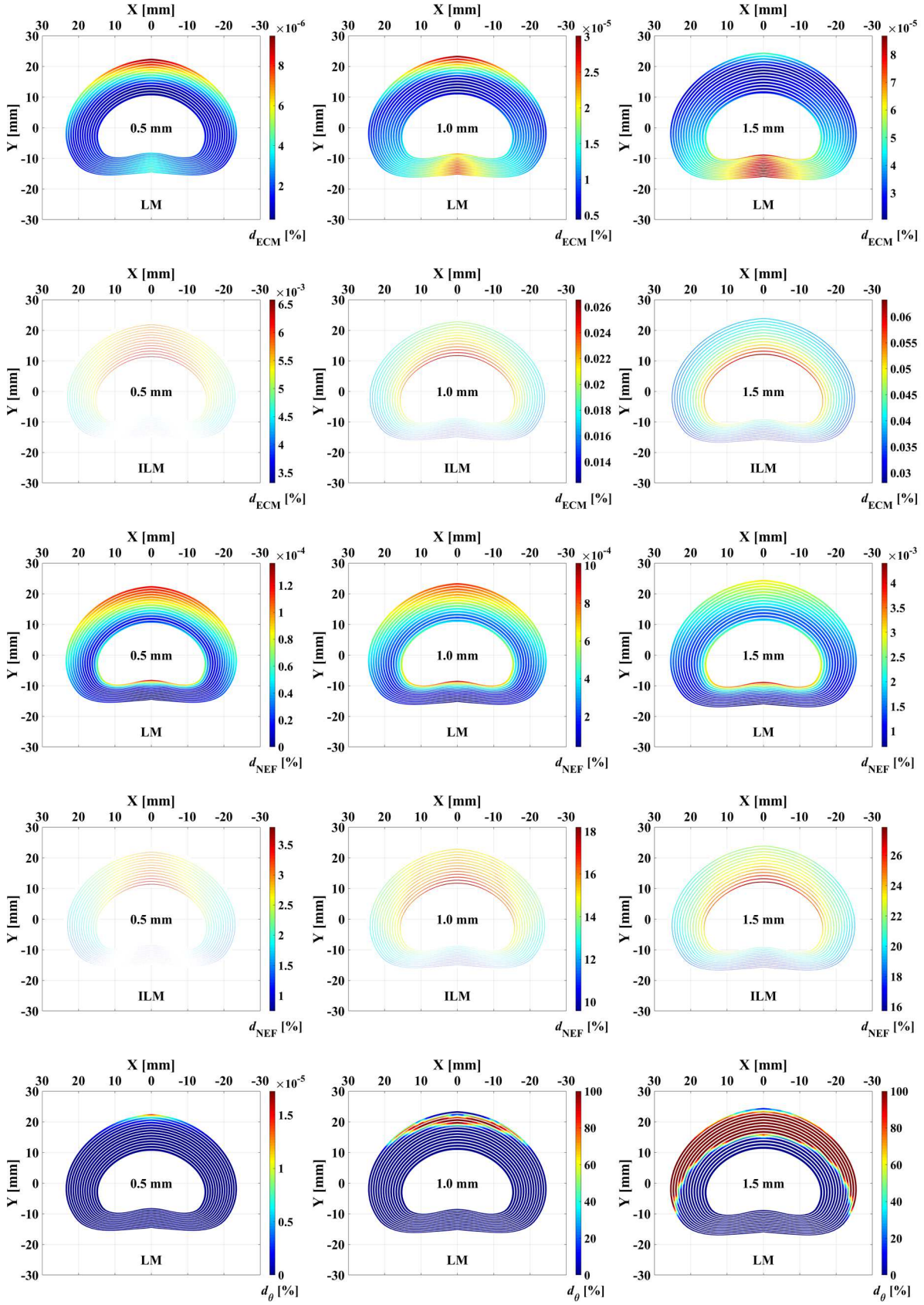

Figure 12. Damage contour plots in the superior view of the uniaxially compressed disc for different applied displacement levels (0.5, 1.0 and 1.5 mm); ECM damage d_{ECM} in LM and in ILM, NEF damage d_{NEF} in LM and in ILM, OCF damage d_{θ} in LM.

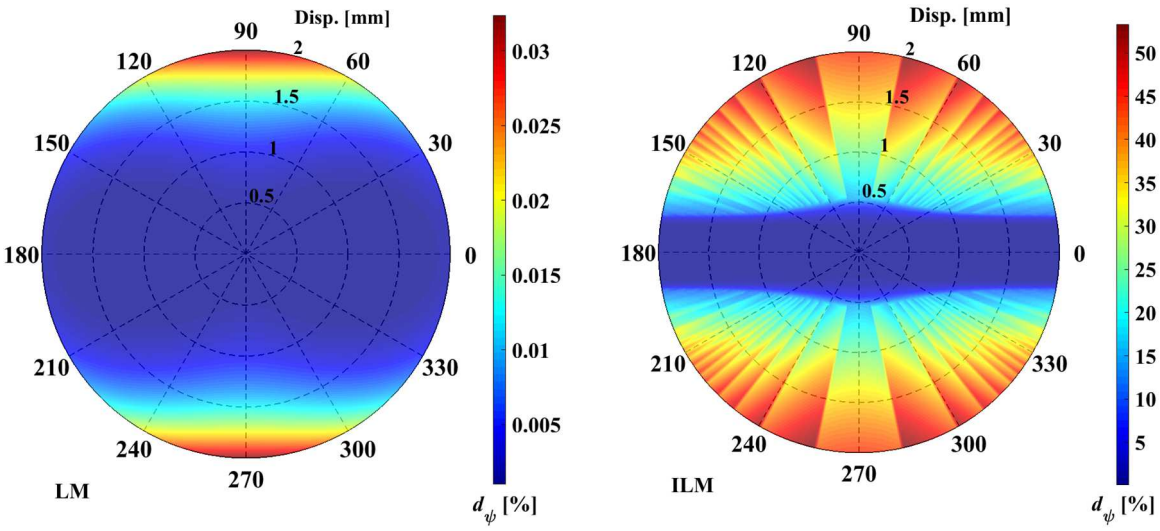

(a) (b)

Figure 13. Damage of the fibrils in different directions (90° is the radial direction) at two zones of the uniaxially compressed disc: (a) posterior (in LM) and (b) anterior (in ILM) sides of the inner annulus for different applied displacement levels (from zero in the dial center to 2 mm in the dial boundary).

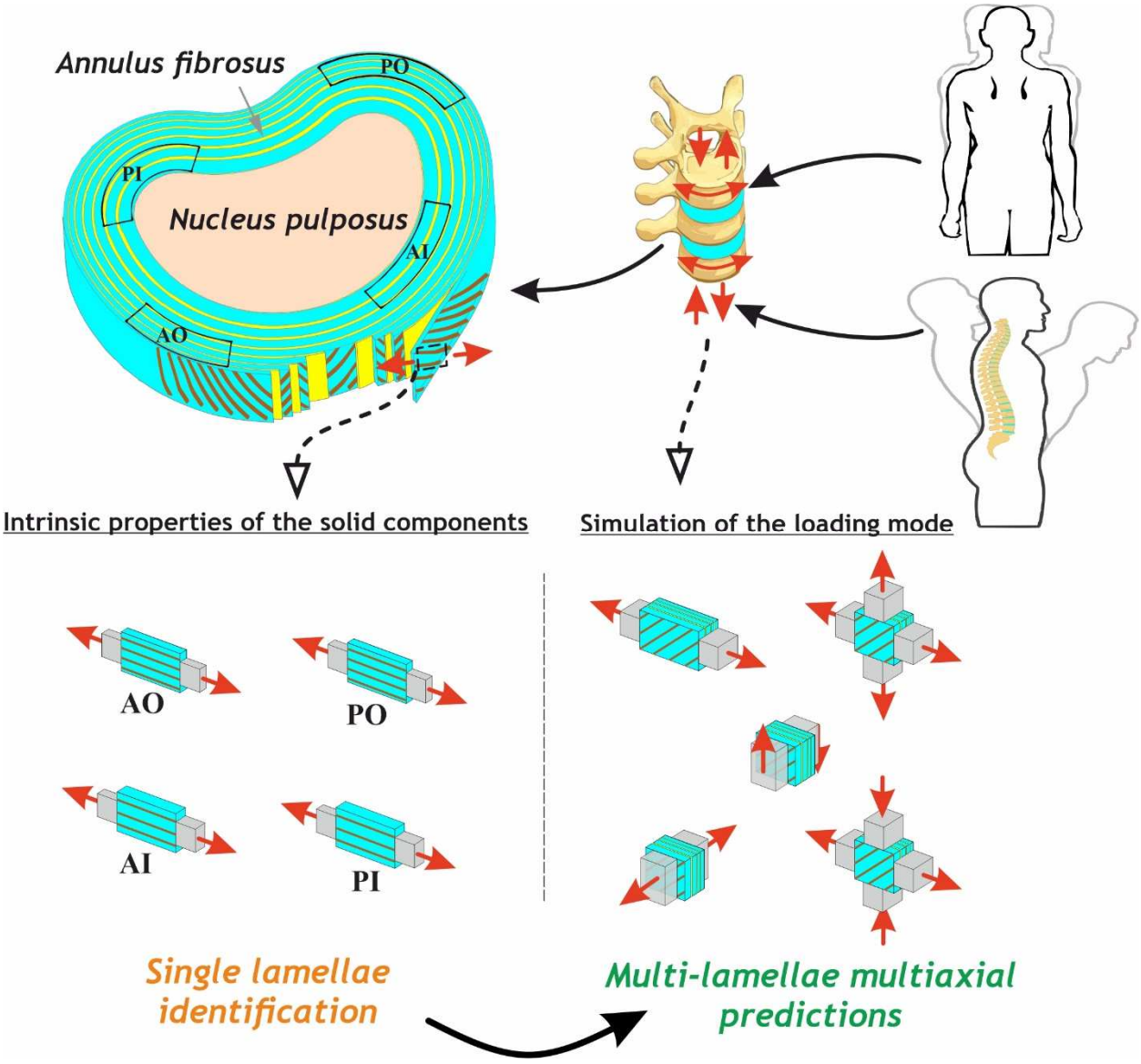
Annulus fibrosus
PO
PI
Nucleus pulposus
AI
AO
Intrinsic properties of the solid components
Simulation of the loading mode
AO
PO
AI
PI
Single lamellae identification
Multi-lamellae multiaxial predictions